CrossMark

JM PAPERS

Interaction between thermal stratification and turbulence in channel flow

Francesco Zonta[1], Pejman Hadi Sichani[1,2] and Alfredo Soldati[1,2,†]

[1]Institute of Fluid Mechanics and Heat Transfer, TU-Wien, 1060 Vienna, Austria
[2]Polytechnic Department, University of Udine, 33100 Udine, Italy

Transport phenomena in high Reynolds number wall-bounded stratified flows are dominated by the interplay between the turbulence structures generated at the wall and the buoyancy-induced large-scale waves populating the channel core. In this study, we want to investigate the flow physics of wall-bounded stratified turbulence at relatively high shear Reynolds number Re_τ and for mild to moderate stratification level – quantified here by the shear Richardson number varying in the range $0 \leqslant Ri_\tau \leqslant 300$. By increasing stratification, active turbulence is sustained only in the near-wall region, whereas intermittent turbulence, modulated by the presence of non-turbulent wavy structures (internal gravity waves), is observed at the channel core. In such conditions, the wall-normal transport of momentum and heat is considerably reduced compared with the case of non-stratified turbulence. A careful characterization of the flow-field statistics shows that, despite temperature and wall-normal velocity fluctuations being very large at the channel centre, the mean value of their product – the buoyancy flux – vanishes for $Ri_\tau \geqslant 200$. We show that this behaviour is due to the presence of a $\sim \pi/2$ phase delay between the temperature and the wall-normal velocity signals: when wall-normal velocity fluctuations are large (in magnitude), temperature fluctuations are almost zero, and *vice versa*. This constitutes a blockage effect to the wall-normal exchange of energy. In addition, we show that the friction factor scales as $C_f \sim Ri_\tau^{-1/3}$, and we propose a new scaling for the Nusselt number, $Nu \cdot Re_\tau^{-2/3} \sim Ri_\tau^{-1/3}$. These scaling laws, which seem to be robust over the explored range of parameters, complement and extend previous experimental and numerical data, and are expected to help the development of improved models and parametrizations of stratified flows at large Re_τ.

Key words: stratified turbulence

† Email address for correspondence: alfredo.soldati@tuwien.ac.at

1. Introduction

A turbulent channel flow heated from the top and cooled from the bottom – so that warm and thus lighter fluid overlays cold and thus heavier fluid – is called stably stratified-turbulent channel flow. This flow is subject to a vertical (wall-normal) buoyancy force that, interacting with turbulence, can strongly change momentum, energy and mass transport. The complex physics of wall-bounded stably stratified turbulence is governed by the interplay between inertial and buoyancy forces, flavoured also by the presence of viscous forces and thermal diffusion. This interplay is commonly quantified in terms of three main dimensionless numbers: the Reynolds number Re – the ratio of inertial to viscous forces – the Richardson number Ri – the ratio of buoyancy to inertial forces – and the Prandtl number Pr – the ratio of momentum to thermal diffusivities. The study of stably stratified turbulence in the presence of boundaries is of great importance in a number of industrial processes, from energy supply/removal in heat transfer equipment to chemical/nuclear reactors (Dostal, Hejzlar & Driscoll 2006; Pitla *et al.* 2006), but it has also significance in a number of environmental flows, including for example the dynamics of the nocturnal atmospheric boundary layer (Mahrt 2014), or the motion of organic matter in terrestrial water bodies (LaCasce & Bower 2000; Lovecchio, Zonta & Soldati 2014).

Since the first works of Monin & Obukhov (1954) and Bolgiano (1959), which were motivated by the study of the atmospheric boundary layer, a number of field measurements, experiments, simulations and theoretical models have been developed (we refer the reader to Fernando (1991), Zonta & Soldati (2018) and Caulfield (2021), for a more complete overview on the topic) with the main purpose of inferring flow stability properties and suitable scaling laws for the relevant global quantities (i.e. energy/momentum fluxes, length scales, mixing efficiency) as a function of the observed/imposed stratification. Reportedly, detailed experimental measurements of stratified flows, in particular in proximity of a wall, are extremely challenging and difficult to realize when non-optical techniques are employed (Arya 1975; Komori *et al.* 1983; Ohya, Neff & Meroney 1997). Yet, accurate measurements by optical techniques have become available recently (Williams *et al.* 2017), and have contributed a lot to the advancement in the field, although their accuracy in the near-wall region remains problematic.

In this context, numerical simulations – granting access to the entire velocity and temperature field down to the region very close to the wall – have emerged as a valuable tool to understand and characterize the local as well as the global structure of the flow. It is therefore not surprising that large eddy simulations and direct numerical simulations (LES and DNS) of thermally stratified channel turbulence have been performed more and more frequently in the last twenty years. Among the first numerical studies of wall-bounded stratified flows, Garg *et al.* (2000) employed wall-resolved LES to compute the dynamics of incompressible stratified turbulence in both closed and open channel flow configurations at a constant Reynolds and Prandtl numbers ($Re_\tau = 180$ and $Pr = 0.71$) but at different Richardson number Ri_τ (i.e. different stratification levels). Note that the subscript τ indicates parameters expressed in wall units, i.e. using the shear velocity u_τ as reference velocity. Based on the value of Ri_τ, the flow was divided into a buoyancy-affected flow ($Ri_\tau < 30$, characterized by general turbulence attenuation), a buoyancy-controlled flow ($30 < Ri_\tau < 45$, with the possibility of transient and local flow relaminarization) and a buoyancy-dominated flow ($Ri_\tau > 45$, with a complete flow relaminarization). Similar trends, showing the occurrence of local flow laminarization, were observed by Iida, Kasagi & Nagano (2002) in their DNS of stratified channel turbulence at similar Reynolds and Richardson numbers ($Re_\tau = 150$, $Ri_\tau \leqslant 40$). As discussed by Armenio & Sarkar (2002),

such findings were, however, in contrast with the linear stability analysis of Gage & Reid (1968) that, compared with the results of Garg *et al.* (2000) and Iida *et al.* (2002), predicted a complete flow laminarization to occur only at much higher values of Ri_τ. A clearcut explanation of this inconsistency was given only later (Moestam & Davidson 2005; García-Villalba & del Álamo 2011). In particular, performing DNS of stratified channel turbulence up to $Re_\tau = 550$ and $Ri_\tau = 960$, and employing large computational domains, García-Villalba & del Álamo (2011) were able to show that the local flow laminarization at subcritical values of Ri_τ occurs when the computational domain is not large enough to contain the minimal flow unit required to sustain turbulence. In such an instance, laminar patches appear, increase in size and become as large as the entire computational domain, hence making a back transition to turbulence – which would be observed in larger computational domains – not possible.

All previous studies were particularly important since they demonstrated not only that the overall momentum and heat transfer rates are reduced for increasing stratification, but also that the structure of wall-bounded turbulence can be selectively modified. The current state of DNS research in the field of stably stratified channel turbulence is summarized in the (Re_τ, Ri_τ) phase space diagram shown in figure 1 (adapted from Zonta & Soldati 2018). The black solid line represents the boundary ideally separating the laminar region (above the curve), from the turbulent one (below the curve). This curve, which has been obtained by best fit of the data reported in Gage & Reid (1968), should not be taken as a sharp boundary between two regimes, but more likely as a blurry transition region in which the flow is expected to (gradually) change behaviour from turbulent to laminar flow. There is indeed strong evidence that, when the marginal stability curve is approached, the flow becomes intermittent (stratification is so strong that laminar patches appear in the near wall region, although the mean flow is still able to sustain turbulence, see García-Villalba & del Álamo 2011; Brethouwer, Duguet & Schlatter 2012). The symbols below the curve represent previous DNS (Iida *et al.* 2002; Moestam & Davidson 2005; Yeo, Kim & Lee 2009; García-Villalba & del Álamo 2011; Zonta, Onorato & Soldati 2012*b*), which reach a maximum Reynolds number $Re_\tau = 550$. Simulations at a larger Reynolds number were performed more recently by other authors (Deusebio, Caulfield & Taylor 2015; Williamson *et al.* 2015; He 2016), but in different flow configurations (i.e. Couette flow or open channel). For weakly to moderate stratification, buoyancy-driven wave-like motions (internal gravity waves, IGWs) appear at the channel core and coexist with classical near-wall turbulence (see inset 'Flow 1' below the curve highlighting the presence of IGW via visualization of temperature contours on a longitudinal section of the channel). In this case, statistics still scale well in wall units. As already mentioned, when stratification is increased so as to approach the marginal stability curve, the situations is more complicated, since buoyancy is able to influence not only the flow region far from the boundary, but also the region close to it. This generally leads to the collapse of near-wall turbulence and to the corresponding appearance of laminar patches. For very strong stratification – stronger than the critical strength dictated by the marginal stability curve – the flow becomes laminar (see inset 'Flow 2' above the curve, showing a complete laminarization of the flow).

With the final aim of assessing the current physical description and corresponding parametrizations of stratified wall-bounded turbulence at high Reynolds numbers, we perform a series of DNS of stably stratified channel flow at $Re_\tau = 1000$, i.e. well beyond the current state-of-the art limit of $Re_\tau = 550$ (see figure 1), and for $0 \leqslant Ri_\tau = 300$. Computations at high Reynolds number are crucial in this field, given the lack of indications that results obtained by low Reynolds number simulations can be upscaled
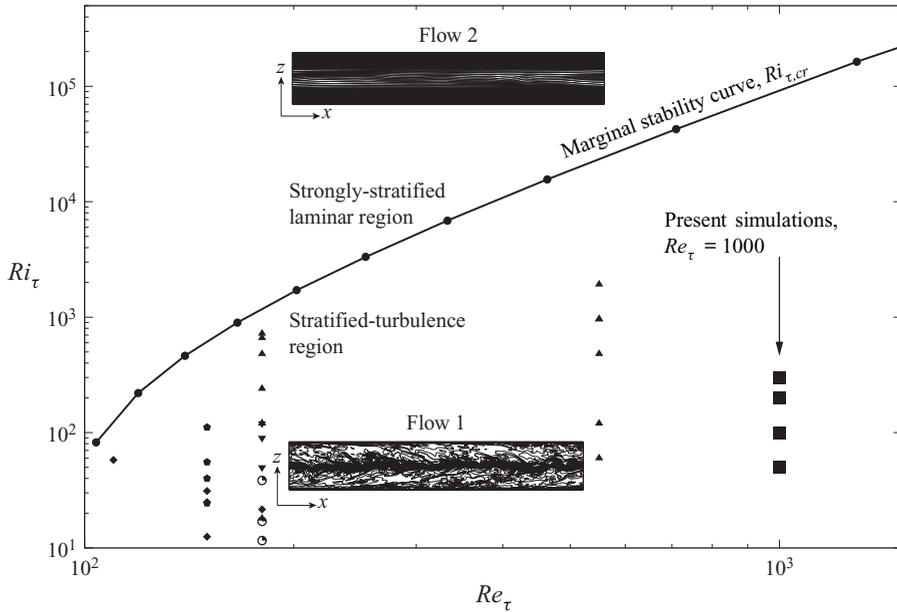
Figure 1. Comprehensive sketch of the (Re_τ–Ri_τ) diagram for stratified turbulence in closed channels (adapted from Zonta & Soldati 2018). Circles represent the critical $Ri_{\tau,cr}$ (marginal stability curve) obtained from the linear stability analysis of Gage & Reid (1968), and properly rearranged to fit for the present parameter space. The proposed parametrization of the marginal stability curve (solid line) is: $\log(Ri_{\tau,cr}) = m \times [\log(Re_\tau)]^b + n \times [\log(Re_\tau) - d]^a + c$, where the value of the parameters is $a = -0.1843$, $b = 1.047$, $c = 1.914$, $d = 1.927$, $m = 1.651$ and $n = -2.204$ (Zonta & Soldati 2018). The symbols below the curve – in the range $0 \leqslant Re_\tau \leqslant 550$ – represent previous DNS found in the literature (Iida *et al.* 2002; Moestam & Davidson 2005; Yeo *et al.* 2009; García-Villalba & del Álamo 2011; Zonta *et al.* 2012b). The simulations performed in this work are indicated by the filled squares (■). The two insets, labelled Flow 1 and Flow 2, are used to visualize the typical flow structure (temperature contours) in the stratified-turbulence region (Flow 1) and in the strongly stratified laminar region (Flow 2).

to the scale of real phenomena, especially in environmental and large-scale industrial applications. The present study represents a first effort in this direction: the detailed dataset produced by the present computationally intensive simulations at high Re_τ, can definitely help LES and Reynolds-averaged Navier–Stokes simulations to develop reliable subgrid-scale and turbulence closure models that properly account for buoyancy effects in realistic applications.

The paper is built as follows. In § 2 we describe the governing equations and the numerical method employed to run the simulations. In § 3, building on top of a detailed analysis of the flow-field structure and statistics, we characterize IGWs from a qualitative and quantitative viewpoint, we discuss the influence of stratification on the wall-normal transport of momentum and heat and we present possible parametrizations and scaling laws for the friction factor and for the Nusselt number. Conclusions are finally drawn in § 4.

2. Methodology

We consider a stably stratified-turbulent flow inside a horizontal straight channel. The origin of the coordinate system is located at the centre of the channel and the x-, y- and z-axes point in the streamwise, spanwise and wall-normal directions, respectively. A stable

stratification in the wall-normal direction z is maintained by keeping a positive temperature difference $\Delta T = T_t - T_b$ between the top (fixed temperature T_t) and the bottom (fixed temperature T_b) walls. At the same time, the flow is driven along the streamwise direction x by an imposed mean pressure gradient. Conservation of mass, momentum and energy, written in dimensionless form and under the Oberbeck–Boussinesq approximation, is

$$\nabla \cdot \boldsymbol{u} = 0, \tag{2.1}$$

$$\frac{\partial \boldsymbol{u}}{\partial t} + (\boldsymbol{u} \cdot \nabla)\boldsymbol{u} = -\nabla p' + \frac{1}{Re_\tau}\nabla^2 \boldsymbol{u} + Ri_\tau \theta \delta_{i,3} + \delta_{1,i}, \tag{2.2}$$

$$\frac{\partial \boldsymbol{\theta}}{\partial t} + (\boldsymbol{u} \cdot \nabla)\theta = \frac{1}{Re_\tau Pr}\nabla^2 \theta, \tag{2.3}$$

where $\boldsymbol{u}$ is the velocity vector, p' is the fluctuating kinematic pressure, $\theta = (T - T_{ref})/(\Delta T/2)$ is temperature and $\delta_{1,i}$ is the mean pressure gradient that drives the flow in the streamwise direction only (note that $\delta_{i,j} = 1$ if $i = j$, while $\delta_{i,j} = 0$ if $i \neq j$). Equations (2.1)–(2.3) have been obtained using the half-channel height h as reference length, the centreline temperature $T_{ref} = (T_t + T_b)/2$ as reference temperature and the shear velocity $u_\tau = \sqrt{\tau_w/\rho}$ as reference velocity – with τ_w the shear stress at the wall. Superscripts, which will be used throughout the paper to indicate dimensionless variables, are omitted in (2.1)–(2.3) for ease of notation. The three main parameters of the flow are the shear Reynolds number $Re_\tau = \rho u_\tau h/\mu$, the shear Richardson number $Ri_\tau = \beta(\Delta T/2)gh/u_\tau^2$ and the Prandtl number $Pr = \mu c_p/\lambda$. The acceleration due to gravity is g. Fluid density ρ, viscosity μ, thermal conductivity λ, specific heat c_p and thermal expansion coefficient β are all evaluated at the reference temperature T_{ref}. Present simulations are run at fixed Reynolds and Prandtl number ($Re_\tau = 1000$ and $Pr = 0.71$) but at different values of the Richardson number $Ri_\tau = 50, 100, 200, 300$. A reference simulation at $Ri_\tau = 0$ (neutrally buoyant) is also performed. From a physical point of view, the simulation set-up can represent the flow of air inside a channel of height $2h \sim 1.5$ m at a reference bulk Reynolds number $Re_b = \rho u_b h/\mu = 2 \times 10^4$ and subject to a wall-to-wall temperature difference up to ≈ 10 K.

The initial conditions for the simulations have been prescribed following the strategy already used in previous investigations (Armenio & Sarkar 2002; García-Villalba & del Álamo 2011). First, we run the preliminary case of the turbulent channel flow at $Re_\tau = 1000$ and $Ri_\tau = 0$ (temperature is a passive scalar), until we converge to a statistically steady state. Then, we use one of the last flow fields of the case at $Ri_\tau = 0$ as initial condition for the simulation at $Ri_\tau = 50$, which we run until convergence to a new statistically steady state. Similarly, we use one of the last flow fields of the simulation at $Ri_\tau = 50$ as initial condition for simulation at $Ri_\tau = 100$, and so on with the other cases. A comprehensive overview of the most important parameters of the simulations is provided in table 1. Note that the size of the computational domain and the spatial resolution, reported in table 1, have been chosen to fulfil the requirements imposed by the DNS. In particular, we explicitly compare the employed grid resolution with the minimum value of the Kolmogorov length scale (occurring at the wall) – computed as $\eta_k = (\nu^3/\epsilon)^{1/4}$, with ϵ the turbulent kinetic energy dissipation and $\nu = \mu/\rho$ the kinematic viscosity – with the grid spacing. Also listed in table 1 is the value of the key response parameters in stratified turbulence, the Nusselt number $Nu = 2q_w h/(\lambda \Delta T)$, with q_w the heat flux at the wall. A thorough discussion on the behaviour of Nu, and of other important macroscopic parameters, will be given in § 3.5.

Simulation	Ri_τ	Re_b	Nu	Grid points	Δx^+	Δy^+	Δz_w^+	Δz_c^+	$\eta_{k,w}^+$
S0	0	19 940	28.15	$1024 \times 1024 \times 1025$	12.2	6.1	0.004	3.1	1.4
S50	50	22 800	9.56	$1024 \times 1024 \times 1025$	12.2	6.1	0.004	3.1	1.4
S100	100	24 040	6.81	$1024 \times 1024 \times 1025$	12.2	6.1	0.004	3.1	1.4
S200	200	26 320	5.27	$1024 \times 1024 \times 1025$	12.2	6.1	0.004	3.1	1.4
S300	300	28 300	4.64	$1024 \times 1024 \times 1025$	12.2	6.1	0.004	3.1	1.4

Table 1. Stably stratified channel turbulence at $Re_\tau = 1000$ and $Pr = 0.71$: summary of the simulation parameters. For all simulations, the size of the computational domain is $4\pi h \times 2\pi h \times 2h$ along x, y and z, respectively. The grid resolution, Δx^+, Δy^+ and Δz^+, is expressed in wall units. While the grid resolution is constant along x and y, it does change in the wall-normal direction from a minimum value close to the wall (Δz_w^+) to a maximum value at the channel centre (Δz_c^+). The value of the Kolmogorov scale at the wall, $\eta_{k,w}^+$, is also given.

The governing equations are discretized using a pseudo-spectral method based on transforming the field variables into wavenumber space, through Fourier representations for the periodic (homogeneous) directions x and y, and Chebyshev representation for the wall-normal (non-homogeneous) direction z. Periodicity along x and y is assumed for both velocity and temperature, while no-slip velocity and imposed-temperature conditions are assumed at the two walls. Time advancement is achieved using an implicit Crank–Nicolson scheme for the diffusive terms and an explicit Adams–Bashforth scheme for the convective/nonlinear terms. As customarily done in pseudo-spectral methods, convective/nonlinear terms are computed in physical space and then transformed to wavenumber space using a dealiasing procedure (2/3 rule). Further details on the numerical method can be found in Zonta, Marchioli & Soldati (2012*a*), Zonta *et al.* (2012*b*) and Zonta & Soldati (2014).

3. Results

3.1. *Qualitative behaviour of the flow structure*

We look first at the qualitative structure of the flow, focusing in particular on the instantaneous temperature distribution θ on a ($y - z$) cross-section of the channel located at $x = L_x/2$. Results, which are shown in figure 2 for $Ri_\tau = 0$ (panel *a*, neutrally buoyant case) and for $Ri_\tau = 300$ (panel *b*, stably stratified case), will be conveniently discussed by keeping the neutrally buoyant case ($Ri_\tau = 0$, figure 2*a*) as reference. For $Ri_\tau = 0$, temperature is a passive scalar and, as such, it is purely transported by velocity. Vortical structures rising from the boundaries are therefore free to travel over long distances, since they are only bounded by the physical constraint imposed by the walls. Under the action of these vortical structures, a fluid particle with a given temperature is brought to a region with a different temperature, where it thermalizes by diffusion (see figure 2*a*). This naturally gives a high degree of mixing. For $Ri_\tau = 300$, the situation is different. While vortical structures are still dominating the near-wall region, their influence away from the boundary appears limited. The reason is that vortical structures are in this case subject to an additional vertical (i.e. in the wall-normal direction) constraint imposed by gravity, which reduces their range of influence to approximately half of the channel height (this is rather clear upon comparison of figure 2*a,b*). As a consequence, the channel results divided into a top, hot part, and a bottom, cold part (figure 2*b*). These two parts behave almost independently each other, and are separated by IGWs (streaky structure developing
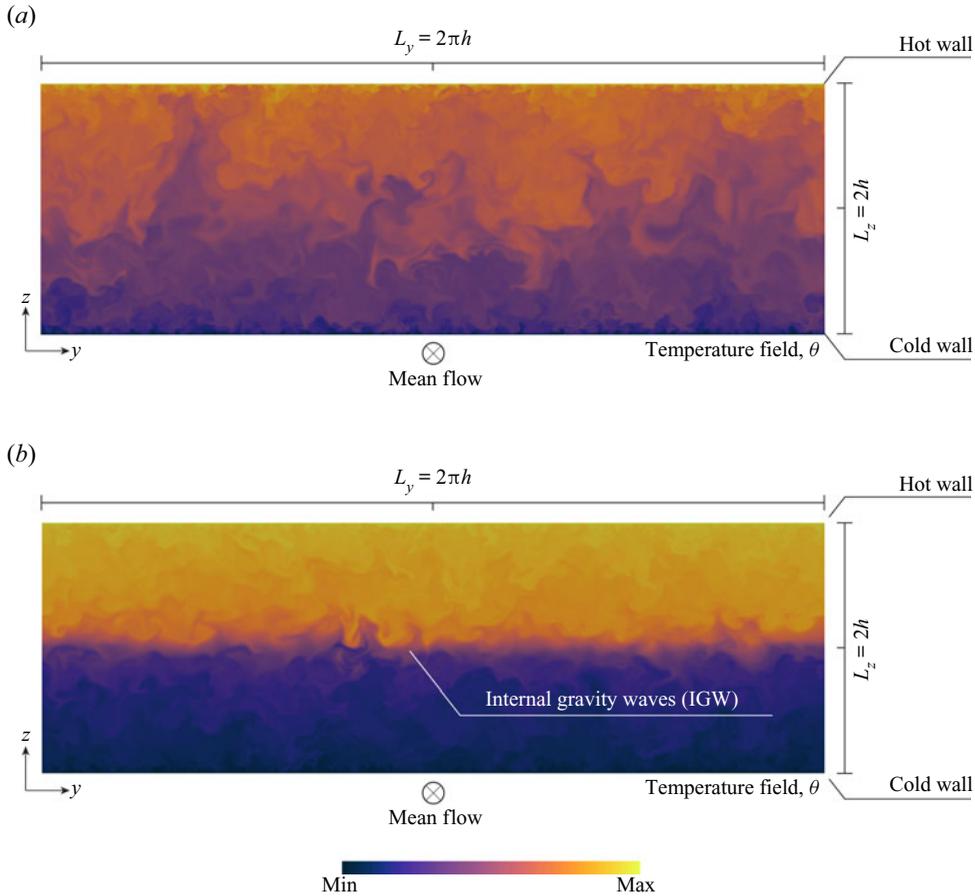
(*a*)

(*b*)

Figure 2. Contour maps of temperature, θ, on a (y–z) cross-section located at $x = L_x/2$. (*a*) Refers to the neutrally buoyant case, $Ri_\tau = 0$ and (*b*) refers to the stably stratified case at $Ri_\tau = 300$.

at the channel centre). The physics of IGWs is simple: because of the background density profile – with density decreasing with height – a fluid particle that is displaced in the wall-normal direction by velocity fluctuations is subject to a restoring buoyancy force that tends to bring it back to its initial position. The fluid particle trespasses its initial equilibrium position and overshoots inertially, giving rise to an oscillation that constitutes the essence of IGWs. We anticipate here, but it will become clear by looking at the fluid statistics in the next paragraphs, that IGWs appear inside a thermocline – i.e. a region where temperature changes much more than it does above and below it, hence representing a sort of thick interface that hinders the wall-normal transfer of momentum and heat. Due to their importance in the dynamics of stably stratified flows, IGWs have been analysed in detail in a number of previous studies (we refer the reader to Staquet & Sommeria (2002), for a comprehensive review on the topic). IGWs will be further characterized from a more quantitative and qualitative viewpoint in § 3.4.

To appreciate the different flow structure induced by the stable stratification, we now turn our attention to the distribution of temperature θ and axial velocity u_x on a longitudinal (x–z) plane located at $y = L_y/2$. Results are shown in figure 3: panel (*a*) and panel (*b*) refer to $Ri_\tau = 0$ (temperature and axial velocity, respectively), while panel (*c*) and

panel (*d*) refer to $Ri_\tau = 300$ (temperature and axial velocity, respectively). The flow moves from left to right. As expected, for $Ri_\tau = 0$, temperature (figure 3*a*) – which is a passive scalar – is efficiently mixed throughout the entire height of the channel by the dominant vortical structures. The flow (figure 3*b*) appears organized into taller vortices which are emitted from the wall and contain ensembles of smaller-scale vortices. The wall-normal extension of these taller vortices scales with the channel height $\sim 2h$. For $Ri_\tau = 300$, on the other hand, the situation is controlled by the presence of IGWs, which – as clearly visible in both the temperature and velocity maps – dominate the central region of the channel. The presence of these structures naturally modifies the entire dynamics of the flow, inducing an extra confinement to the wall-normal development of vortices, and reducing at the same time their capability of effectively mixing the flow. As a side observation, we note that the temperature field in the proximity of the channel centre appears stretched and tilted at an angle with respect to the horizontal direction. This is due to the presence of a strong vertical shear in that region.

3.2. *Velocity and temperature statistics*

We now characterize the flow from a statistical viewpoint. Unless differently stated, all results will be presented in wall units (denoted by superscript $+$), obtained normalizing velocities by u_τ, lengths by $l_\tau = \nu/u_\tau$, times by $t_\tau = \nu/u_\tau^2$ and temperatures by $\theta_\tau = q_w/u_\tau$. In figure 4 we show the behaviour of the mean streamwise velocity $\langle u_x^+ \rangle$ as a function of the wall-normal coordinate, in linear (figure 4*a*) and semilog (figure 4*b*) scale. Brackets indicate time and space average over the homogeneous directions. Results are rendered according to the following colour code: blue (up-triangle) refers to the neutrally buoyant case ($Ri_\tau = 0$), yellow (down-triangle) refers to $Ri_\tau = 50$, green (square) refers to $Ri_\tau = 100$, purple (diamond) refers to $Ri_\tau = 200$ and red (circle) refers to $Ri_\tau = 300$. The law of the wall, $\langle u_x^+ \rangle = z^+$, and $\langle u_x^+ \rangle = (1/\kappa) \log(z^+) + 5.5$, with κ the von Kármán constant, is also shown in figure 4(*b*) by a solid line. As expected (see in particular figure 4*b*), in the neutrally buoyant case the mean velocity closely follows the law of the wall, since temperature is a passive scalar that does not influence the velocity field. In the stably stratified cases, we observe an increase of the mean axial velocity, which is particularly pronounced in the core part of the channel (see both figure 4*a,b*), as the shape of the velocity profile deviates significantly from the classical logarithmic behaviour and approaches a nearly laminar, parabolic shape (García-Villalba & del Álamo 2011). This tendency towards a laminarization in the core part of channel is due to the conversion of turbulent kinetic into potential energy, which occurs when a fluid particle moves in the wall-normal direction within the flow. Note also that, since the mean pressure gradient is kept constant among the different simulations, the mean wall stress remains constant, and so does the slope of the velocity at the wall, with all profiles collapsing onto that of the neutrally buoyant case ($z^+/h^+ < 0.1$).

As shown in figure 5, stratification modifies the behaviour of the mean temperature field $\langle\theta\rangle$, which takes a layered structure formed by a near-wall layer ($0 < z^+/h^+ < 0.1$), a transition layer ($0.1 < z^+/h^+ < 0.8$) and a core layer ($0.8 < z^+/h^+ < 1$). Note that temperature in figure 5(*a*) is shown in outer units, i.e. not rescaled in wall units. Compared with the neutrally buoyant case, stratification reduces the mean temperature gradient in the near-wall layer (i.e. it reduces the Nusselt number), while at the same time increasing it in the core layer. This latter observation is of particular importance, since it indicates the tendency for turbulent stratified channel flows to develop a kind of thick interface – the thermocline – inside which the temperature changes more vigorously than it does
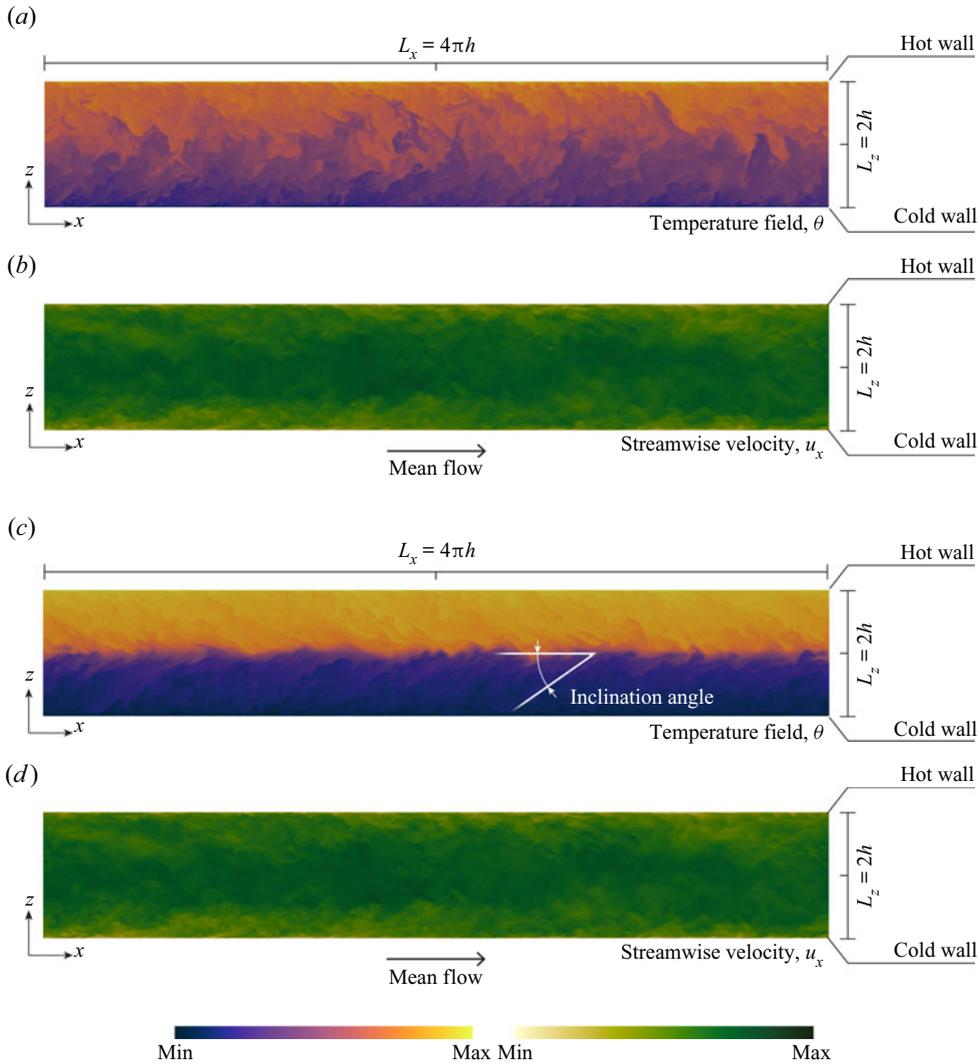
Figure 3. Contour maps of temperature θ (a,c) and streamwise velocity u_x (b,d) on a (x–z) longitudinal section located at $y = L_y/2$. (a,b) Refer to the neutrally buoyant case, $Ri_\tau = 0$ and (c,d) refer to the stably stratified case at $Ri_\tau = 300$. The temperature tilting induced by the vertical shear at the channel centre is also explicitly indicated (c).

immediately above and below. The thermocline, which forms right where the mean shear vanishes, constitutes a barrier for wall-normal momentum and heat transport. Reportedly (Ferziger, Koseff & Monismith 2002; García-Villalba & del Álamo 2011; Zonta *et al.* 2012*b*; Zonta & Soldati 2018), there is a strong connection between the presence of a thermocline and the presence of IGWs (which, as discussed in § 3.1, occur at the channel centre), in the sense that IGWs develop where a thermocline exists. Interestingly, the temperature gradient in the core region of the channel does not increase monotonically for increasing Ri_τ: it first increases (going from $Ri_\tau = 0$ to $Ri_\tau = 100$), and then reduces (going from $Ri_\tau = 100$ to $Ri_\tau = 300$). We anticipate here, but we will come back to it later, that this non-monotonic trend of the temperature profile at the channel centre can be explained by looking at the intertwined behaviour of the turbulent (or buoyancy)
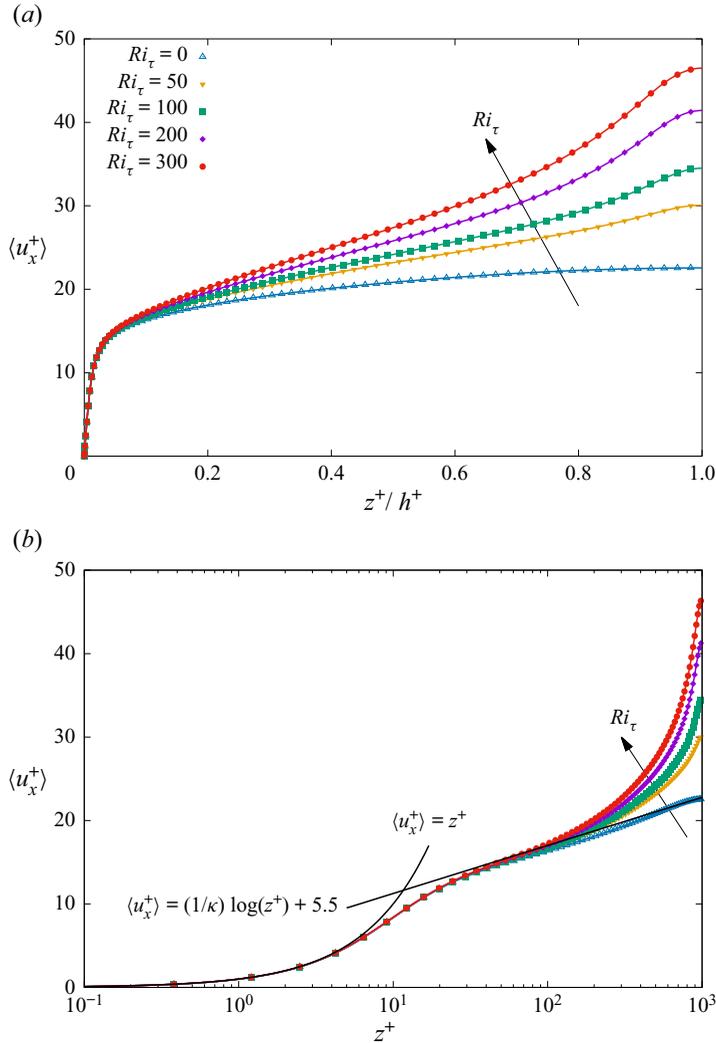
Figure 4. Mean fluid streamwise velocity $\langle u_x^+ \rangle$ as a function of the wall-normal direction, z^+, in linear (*a*) and semilog scale (*b*) for the different cases considered in the present study. Comparison between the reference case of unstratified turbulence ($Ri_\tau = 0$), and the stratified turbulence at $Ri_\tau = 50$, $Ri_\tau = 100$, $Ri_\tau = 200$ and $Ri_\tau = 300$ (filled symbols). The classical law of the wall $\langle u_x^+ \rangle = z^+$ and $\langle u_x^+ \rangle = (1/\kappa) \log(z^+) + 5.5$, with κ the von Kármán constant, is also shown for comparison in (*b*) (solid line).

and diffusive fluxes. In the transition layer, between the near-wall and the core layers, the temperature gradient remains small, as the flow is characterized by a higher degree of mixing. Not surprisingly, when rescaled in wall units, i.e. by keeping the friction temperature $\theta_\tau = q_w/(\rho c_p u_\tau)$ as reference, the mean temperature profile $\Theta^+ = (\theta - \theta_w)/\theta_\tau$ recovers a monotonic behaviour (figure 5*b*). This is particularly visible in the inset of figure 5(*b*), where a close-up view of the mean temperature profile in the core region of the channel is given. Note also that, for the neutrally buoyant case, and similarly to what happens for the streamwise velocity $\langle u_x^+ \rangle$, the behaviour of Θ^+ can be parameterized by $\Theta^+ = Pr \cdot z^+$, in the boundary layer, and by $\Theta^+ = 2.3 \log(z^+) + 3.11$, in the core region (see Alcántara-Ávila *et al.* 2021).
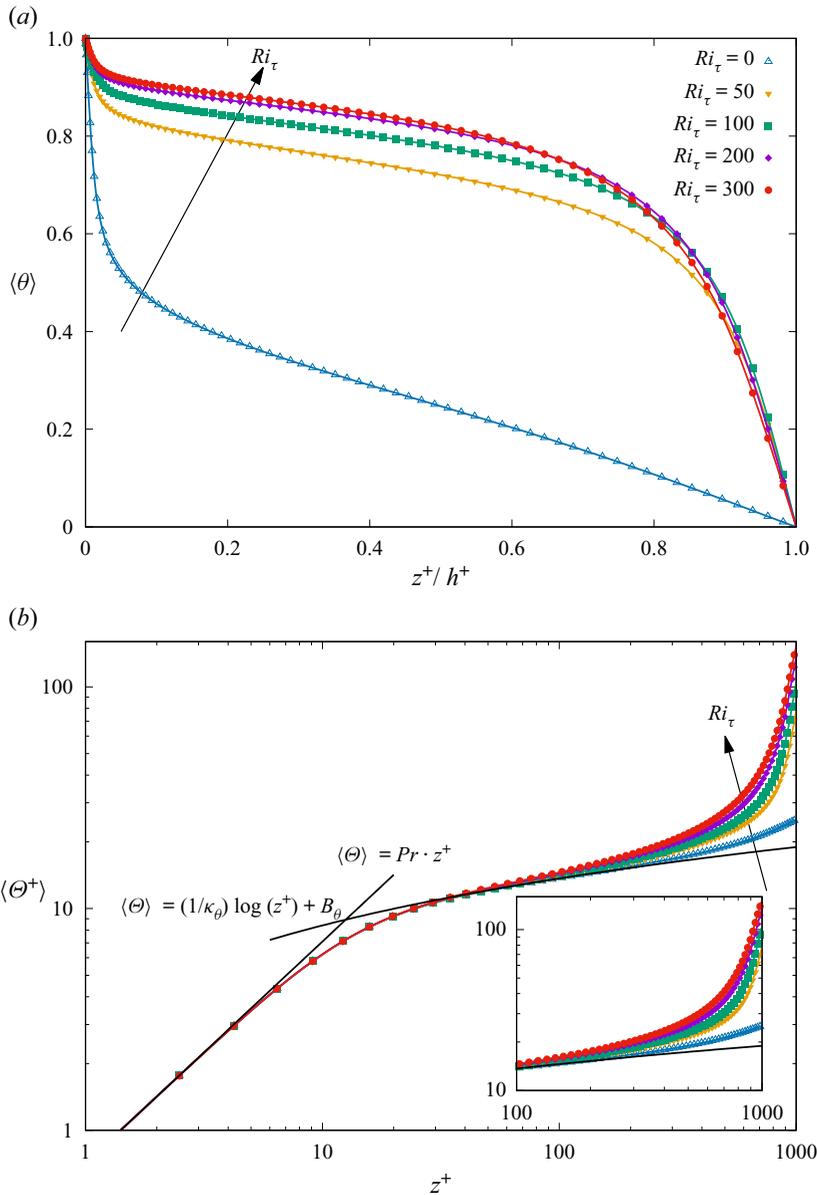
945 A3-10

(*a*)

(*b*)

Figure 5. Mean fluid temperature $\langle\theta\rangle$ in linear (*a*) and log (*b*) scale as a function of the wall-normal distance expressed in wall units, z^+. Comparison between the reference case of unstratified turbulence ($Ri_\tau = 0$), and the stratified turbulence at $Ri_\tau = 50$, $Ri_\tau = 100$, $Ri_\tau = 200$ and $Ri_\tau = 300$ (filled symbols). The correlation $\langle\Theta^+\rangle = Pr \cdot z^+$ and $\langle\Theta^+\rangle = (1/\kappa)\log(z^+) + B_\theta$, with coefficients $\kappa_\theta = 0.436$ and $B_\theta = 3.11$ taken from Alcántara-Ávila, Hoyas & Jezabel Pérez-Quiles (2021), is also shown for comparison (solid line, *b*). A close-up view of the mean temperature in the core region of the channel is offered in (*b*) for clarity.

To evaluate the influence of stratification on turbulence, we now look at the root mean square of the streamwise $\langle u'^+_{x,rms}\rangle$, spanwise $\langle u'^+_{y,rms}\rangle$ and wall-normal $\langle u'^+_{z,rms}\rangle$ velocity fluctuations, and at the root mean square of temperature fluctuations $\langle\Theta'^+_{rms}\rangle$. Results, which are presented in figure 6, clearly show that all velocity and temperature fluctuations are essentially unaffected by stratification in the near-wall region ($z^+/h^+ < 0.1$), where

945 A3-11

they recover the behaviour of canonical near-wall turbulence. Farther from the wall, in the region $0.3 < z^+/h^+ < 0.8$, $\langle u'^+_{x,rms} \rangle$ decreases first and increases later compared with the neutrally buoyant case, while the opposite behaviour – increasing first and decreasing later – is observed for $\langle u'^+_{z,rms} \rangle$. Note that the cross-over between the profiles of stratified and neutrally buoyant turbulence occurs around $z^+/h^+ \simeq 0.5$, and is somehow influenced by Ri_τ. In contrast, $\langle u'^+_{y,rms} \rangle$ is characterized by a clear increase that – provided $Ri_\tau > 0$ – seems independent of the value of Ri_τ. This behaviour, and in particular the increase of $\langle u'^+_{x,rms} \rangle$ and $\langle u'^+_{y,rms} \rangle$, is associated with the increase of velocity gradient (see also figure 7(a) and the discussion therein) in that region, which enhances turbulence production, while the corresponding decrease of $\langle u'^+_{z,rms} \rangle$ is due to the conversion of turbulent kinetic energy (in the vertical direction) into potential energy. In the core region of the channel, $z^+/h^+ > 0.8$, $\langle u'^+_{x,rms} \rangle$ strongly decreases while $\langle u'^+_{z,rms} \rangle$ develops a peak that is not visible in neutrally buoyant turbulence and is due to the presence of IGWs. Correspondingly, a marked peak at the channel centre is also observed for the temperature fluctuations, figure 6(d). Note that, for $\langle \Theta'^+_{rms} \rangle$, there is a clear cross-over between the different cases of stratified turbulence: for increasing Ri_τ, temperature fluctuations tend to increase in the transition layer, $0.1 < z^+/h^+ < 0.8$, and decrease in the core layer $0.8 < z^+/h^+ < 1$ (although they remain much larger than the neutrally buoyant case). To summarize, previous observations indicate that the structure of turbulence is not influenced near the wall, since velocity fluctuations, and also the ratio between the wall-normal and the streamwise velocity fluctuations, $\langle u'^+_{z,rms} \rangle / \langle u'^+_{x,rms} \rangle$, remains almost constant among the different cases. At the same time, in the buffer region there is a decrease of $\langle u'^+_{z,rms} \rangle / \langle u'^+_{x,rms} \rangle$, which indicates that stratification hinders the energy transfer from the streamwise to the wall-normal component. Then, at the channel centre, velocity and temperature fluctuations are essentially induced by IGWs.

3.3. *Momentum and heat fluxes*

We focus here on the wall-normal behaviour of momentum and heat fluxes, two key quantities in turbulent transport phenomena. The momentum flux can be obtained from the Reynolds-averaged streamwise momentum equation as

$$\tau_{tot} = 1 - \frac{2z^+}{Re_\tau} = \underbrace{\frac{\partial \langle u_x^+ \rangle}{\partial z^+}}_{\tau^v_{xz}} + \underbrace{\langle u'^+_x u'^+_z \rangle}_{\tau^t_{xz}}, \tag{3.1}$$

where the turbulent (τ^t_{xy}) and viscous (τ^v_{xy}) counterparts to the overall stress are explicitly indicated. The behaviour of τ^t_{xy} and τ^v_{xy} (symbols) is shown in figure 7(a), together with the behaviour of τ_{tot} (solid black line). Increasing Ri_τ, we note a general reduction of τ^t_{xy}, in particular in the core region, where $\langle u'^+_x u'^+_z \rangle \simeq 0$ for $Ri_\tau \geqslant 200$. Accordingly, a corresponding increase of τ^v_{xy} – and hence of the velocity gradient $\partial u_x / \partial z$ – is observed, so that the overall linear behaviour of the total shear stress is recovered (3.1). This is clearly visualized in the inset of figure 7(a), where a close-up view of the behaviour of τ^t_{xy} and τ^v_{xy} at the channel centre, $0.8 < z^+/h^+ < 1$, is given. In view of the present results, it is clear that the velocity increase observed at the channel centre (see figure 4) is due to the reduction of turbulent momentum flux in the wall-normal direction (i.e. reduction of $u'_x u'_z$), and to the corresponding increase of the relative importance of τ^v_{xy} therein (Armenio & Sarkar 2002; Yeo *et al.* 2009).
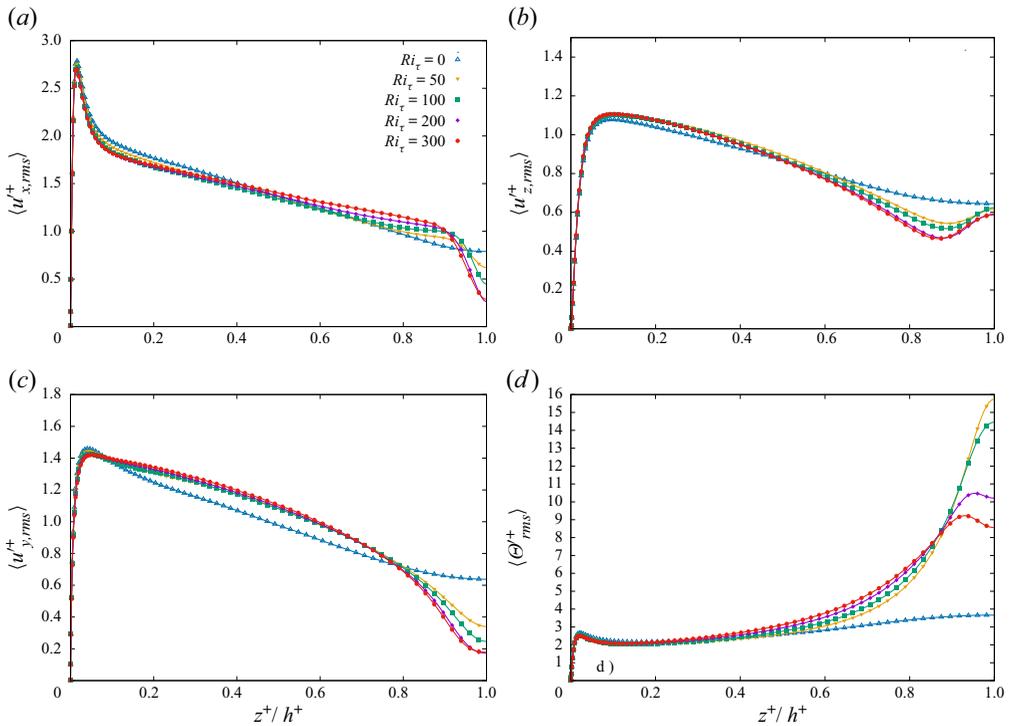
945 A3-12

Figure 6. Wall-normal behaviour of the root mean square of the velocity fluctuations in the streamwise direction ($\langle u'^{+}_{x,rms}\rangle$, panel a), in the spanwise direction ($\langle u'^{+}_{y,rms}\rangle$, panel b) and in the wall-normal direction ($\langle u'^{+}_{z,rms}\rangle$, panel c). The wall-normal behaviour of the temperature fluctuations is also shown ($\langle \Theta'^{+}_{rms}\rangle$, panel d). Comparison between the reference case of unstratified turbulence ($Ri_\tau = 0$), and the stratified turbulence at $Ri_\tau = 50$, $Ri_\tau = 100$, $Ri_\tau = 200$ and $Ri_\tau = 300$ (filled symbols).

Linked to the previous analysis of the wall-normal momentum flux, we now consider the wall-normal heat flux, whose behaviour can be obtained from the Reynolds-averaged energy balance equation as

$$\langle u'_z \theta' \rangle - \alpha \frac{\partial \langle \theta \rangle}{\partial z} = -\alpha \left[\frac{\partial \langle \theta \rangle}{\partial z} \right]_w = q_w, \tag{3.2}$$

where $\alpha = \nu/Pr$ is the thermal diffusivity. Normalizing (3.2) by $q_w = -\alpha[\partial \theta/\partial z]_w$, and recalling that $q_w = \theta_\tau u_\tau$, we finally obtain (Armenio & Sarkar 2002; García-Villalba & del Álamo 2011)

$$\frac{\langle u'_z \theta' \rangle}{q_w} - \frac{\alpha \dfrac{\partial \theta}{\partial z}}{q_w} = \underbrace{\langle u'^{+}_z \Theta'^{+} \rangle}_{q_t} - \underbrace{\frac{1}{Pr} \frac{\partial \langle \Theta^+ \rangle}{\partial z^+}}_{q_d} = 1. \tag{3.3}$$

The two terms q_t and q_d, explicitly indicated in (3.3), represent the turbulent (usually referred to as buoyancy flux) and the diffusive counterparts to the total heat flux, and their behaviour is shown in figure 7(b). By looking at the profile of q_t, it is apparent that, while moving away from the wall – and no matter the value of Ri_τ – q_t increases sharply until it reaches a maximum value of approximately $q_t \simeq 0.95$ around $z^+/h^+ \simeq 0.1$. In neutrally buoyant conditions, this peak value is kept almost unaltered throughout the entire
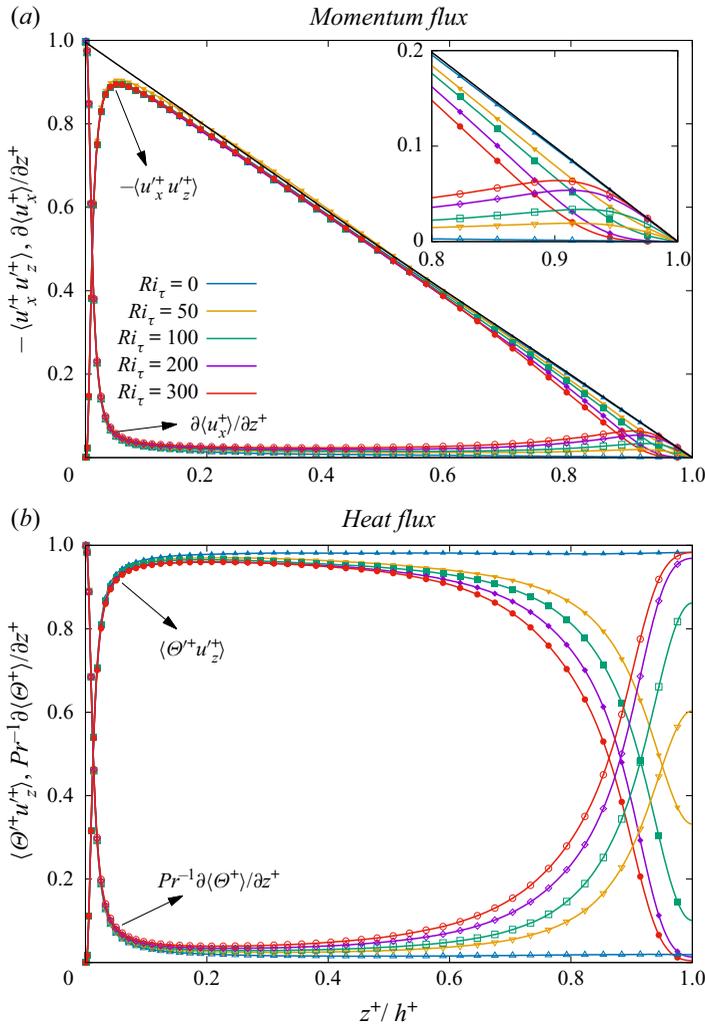
Figure 7. (*a*) Wall-normal behaviour of the viscous shear stress, $\tau_{xy}^v = \partial\langle u_x^+\rangle/\partial z^+$ and turbulent shear stress, $\tau_{xy}^t = \langle u_x'^+ u_z'^+\rangle$. The linear behaviour of the total shear stress, $\tau_{tot}/(\rho u_\tau^2)$ is also shown by the black solid line. Comparison between the reference case of unstratified turbulence ($Ri_\tau = 0$), and the cases of stratified turbulence at $Ri_\tau = 50$, $Ri_\tau = 100$, $Ri_\tau = 200$ and $Ri_\tau = 300$ (filled symbols). (*b*) Wall-normal behaviour of the diffusive heat flux, $q_d = Pr^{-1}\partial\langle\Theta^+\rangle/\partial z^+$ and turbulent heat flux (buoyancy flux), $q_t = \langle u_z'^+\Theta'^+\rangle$. Comparison between the reference case of unstratified turbulence ($Ri_\tau = 0$), and the cases of stratified turbulence at $Ri_\tau = 50$, $Ri_\tau = 100$, $Ri_\tau = 200$ and $Ri_\tau = 300$ (filled symbols).

channel, clearly corresponding to the constant flux hypothesis customarily assumed in neutral boundary layers (Tennekes & Lumley 1972; Ortiz-Suslow *et al.* 2021). At larger Ri_τ, we observe a significant decrease of q_t in the core region of the channel. This decrease is so important that, for $Ri_\tau > 200$, $q_t \simeq 0$. Interestingly, and in agreement with previous observations (Ohya *et al.* 1997; García-Villalba & del Álamo 2011), we cannot find evidence of the speculated mean counter-gradient flux (or, in other words, negative q_t) at the centre of the channel (Komori *et al.* 1983; Armenio & Sarkar 2002).

We further observe that previous studies discussing the possibility of a mean counter-gradient flux considered low-Re_τ flows. Here, we focus on flows at much higher

Re_τ, for which the energy containing boundary layer structures cannot reach very far from the wall. Since we may assume that the mean counter-gradient flux is the outcome of a number of local counter-gradient events (uncorrelated thermal and flow structures) driven by the interaction between near-wall structures and IGW, it is unlikely that a mean counter-gradient flux can be observed at high Re_τ. However, we cannot exclude the presence of a mean counter-gradient flux in strongly stratified conditions, when the flow becomes largely inhomogeneous and intermittent. Between the near-wall and the core regions of the channel there is a region in which q_t remains almost constant and close to unity for all cases considered here, with only a slight decrease for increasing Ri_τ. The diffusive heat flux q_d has a mirror-like behaviour compared with q_t, since the total heat flux is constant across the channel (see (3.3)): q_d decreases sharply while moving away from the wall and it subsequently increases – with the only exception of $Ri_\tau = 0$, for which it remains uniform and very low – in the core region of the channel. This trend of q_d is important to explain the non-monotonic behaviour of the temperature profile observed in figure 5 (q_d is, by definition, proportional to the mean temperature gradient). Note indeed that the mean temperature gradient along the wall-normal direction can be conveniently expressed as (Armenio & Sarkar 2002)

$$\frac{\partial \langle \theta \rangle}{\partial z} = \left[\frac{\partial \langle \theta \rangle}{\partial z} \right]_w \left[1 - \frac{\langle u'_z \theta' \rangle}{u_\tau \theta_\tau} \right], \tag{3.4}$$

where $[\partial \langle \theta \rangle / \partial z]_w$ is the dimensionless mean temperature gradient at the wall, i.e. the Nusselt number. Equation (3.4), together with the observation that the buoyancy flux $q_t = \langle u'_z \theta' \rangle / u_\tau \theta_\tau = \langle u_z'^+ \Theta'^+ \rangle$ becomes almost zero for $Ri_\tau > 200$ (see figure 7b), indicates that for large stratification the temperature gradient at the channel centre perfectly matches the temperature gradient at the wall. Since the temperature gradient at the wall (i.e. the Nusselt number) decreases for increasing Ri_τ, the same does the temperature gradient at the channel centre (but only once Ri_τ is large enough for q_t to be approximately zero). To summarize, the temperature gradient at the channel centre initially increases for increasing stratification, until the stratification becomes so strong to completely damp the turbulent heat transfer (buoyancy flux), i.e. $q_t = \langle u_z'^+ \Theta'^+ \rangle \simeq 0$, at the channel centre. When it happens, the temperature gradient at the channel centre – which becomes equal to the temperature gradient at the wall (Nusselt number) – decreases for increasing Ri_τ.

Despite the large fluctuations of temperature and wall-normal velocity observed around the channel centre for increasing Ri_τ (figure 6c,d), the buoyancy flux $\langle u_z'^+ \Theta'^+ \rangle$ reduces remarkably down to the point at which, for $Ri_\tau \geqslant 200$, it completely vanishes. To understand the reason behind this behaviour, we focus on the distribution of temperature, Θ'^+, and wall-normal velocity fluctuations, $u_z'^+$, on a wall-parallel plane $(x–y)$ located at the channel centre. This is shown in figure 8 for $Ri_\tau = 0$ and $Ri_\tau = 300$. While for $Ri_\tau = 0$ (figure 8a,b), the picture displays the typical features of fully developed turbulence, with spots of positive and negative temperature and wall-normal velocity randomly distributed over the considered plane, for $Ri_\tau = 300$ (figure 8c,d) the situation is different, and there seems to be a connection between Θ'^+ and $u_z'^+$, which are both organized into stripes extending along the spanwise direction y. However, stripes of $u_z'^+$ appear to lag behind those of Θ'^+. The phase lag between $u_z'^+$ and Θ'^+ distributions can be estimated by looking at the coherency spectrum

$$C_{u_z'^+, \Theta'^+}(\kappa_w) = \int_{-\infty}^{\infty} R_{u_z'^+, \Theta'^+}(s) \exp\left(-2\pi j s \kappa_w\right) ds, \tag{3.5}$$
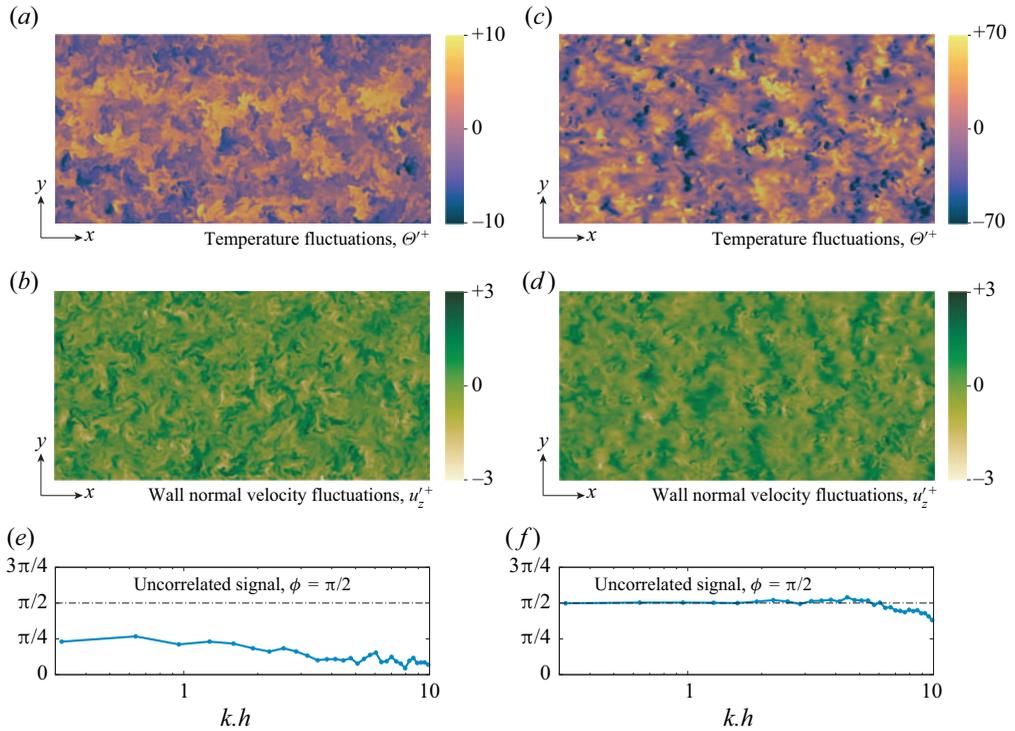
Figure 8. Temperature and velocity fluctuations on a wall-parallel $(x–y)$ plane located at the channel centre for $Ri_\tau = 0$ (a,b) and for $Ri_\tau = 300$ (c,d). Phase of the cross-spectrum, $\phi(C_{u_z'^+,\Theta'^+})$, as a function of the wavenumber $\kappa_w = kh$ for $Ri_\tau = 0$ (e) and for $Ri_\tau = 300$ (f).

with $\kappa_w = kh$ the dimensionless wavenumber and $R_{u_z'^+,\Theta'^+}$ the correlation coefficient between $u_z'^+$ and Θ'^+. In particular, it is intriguing to focus on the phase of $C_{u_z'^+,\Theta'^+}(\kappa_w)$. As shown in figure 8($f$), we clearly notice that, for $Ri_\tau = 300$, $u_z'^+$ and Θ'^+ are shifted by $\pi/2$ (see Iida *et al.* 2002). Such a phase delay is instead not observed at $Ri_\tau = 0$ (see figure 8e). It is important to note that the presence of this phase shift explains why, although temperature and wall-normal fluctuations are both very large at the channel centre, their correlation – that is, the buoyancy flux $\langle u_z'^+\Theta'^+ \rangle$ – is almost zero: where Θ'^+ is maximum in magnitude, $u_z'^+ \simeq 0$ and *vice versa*, consistently with the presence of a wavy motion (IGW).

Not only the average value of the buoyancy flux q_t is important, but also its distribution in space and time. To understand it, we focus on the two limiting cases $Ri_\tau = 0$ and $Ri_\tau = 300$ and we look at the behaviour of q_t on a wall-parallel plane $(x–y)$ located at the channel centre (figure 9a,b), and normalized by the corresponding maximum value $q_{t,max}$ observed on that plane. Then, we compute the probability density function $\Pi(q_t/q_{t,max})$ (figure 9c). For $Ri_\tau = 0$ (blue line in figure 9c), $\Pi(q_t/q_{t,max})$ is highly asymmetric, with the most probable value occurring for $q_t/q_{t,max} = 0$ and with larger positive fluctuations compared with negative ones. This suggests that, although the mean temperature difference between the walls induces a net positive wall-normal energy flux (i.e. the mean value $\langle u_z'^+\Theta'^+ \rangle > 0$), $u_z'^+\Theta'^+$ can often be negative, indicating the presence of regions characterized by local counter-gradient heat fluxes. The occurrence of localized counter-gradient heat fluxes is an extremely important phenomenon that has been observed
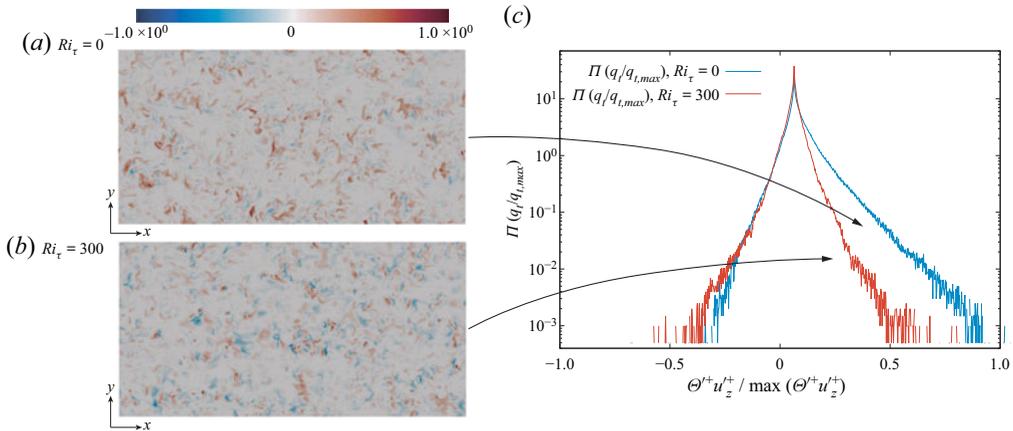
945 A3-16

Figure 9. Contour map of the turbulent heat flux $q_t = \langle \Theta^+ u_z'^+ \rangle$ on a wall-parallel (x–y) plane located at the channel centre for $Ri_\tau = 0$ (*a*), for $Ri_\tau = 300$ (*b*) and corresponding probability density function $\Pi(q_t/q_{t,max})$ (*c*).

also in other situations (Huisman *et al.* 2012; Zonta & Chibbaro 2016; Hadi Sichani *et al.* 2020). From a physical point of view, small positive and negative values of $\Theta'^+ u_z'^+$ are due to turbulence, which is characterized by uncorrelated velocity and temperature fluctuations. These small positive and negative values of $\Theta'^+ u_z'^+$, which are equally likely events, balance each other and do not contribute to the net heat transport (Shang, Tong & Xia 2005). Only large velocity and temperature fluctuations produced by larger coherent structures are correlated and contribute to the net heat flux. And clearly, large positive fluctuations are larger than negative ones, so to produce a positive net heat flux.

The asymmetry of $\Pi(q_t/q_{t,max})$ is almost completely absent at $Ri_\tau = 300$. In particular, while the probability of observing positive fluctuations is globally reduced (i.e. there is a reduction of large correlated velocity and temperature fluctuations), negative fluctuations are rather persistent, so that the average value of $q_t/q_{t,max}$ is close to zero. This is nicely rendered by the contour maps of $q_t/q_{t,max}$ shown in figure 9(*b*): while most of the plane is characterized by a correlation $q_t/q_{t,max} \approx 0$ (and corresponding to the most probable value of $\Pi(q_t/q_{t,max})$ in figure 9), small and rare patches of large positive $q_t/q_{t,max}$ coexist with small and rare patches of large negative $q_t/q_{t,max}$.

3.4. *Internal gravity waves*

In the previous chapter, we described IGWs on a qualitative basis (see in particular figures 2–3 and comments therein). To characterize such structures on a more quantitative basis, we introduce here the buoyancy frequency N (or Brunt–Väisälä frequency), which represents the frequency of oscillation – in a stratified medium – of a lump of fluid that is displaced by velocity fluctuations in the wall-normal direction. In dimensionless form, it is defined as

$$\mathcal{N} = Nh/u_\tau = \sqrt{-g\beta \frac{\partial \langle \theta \rangle}{\partial z} \frac{h}{u_\tau}}, \tag{3.6}$$

and can naturally be used to evaluate the characteristic frequency of oscillation of IGWs. The behaviour of $\mathcal{N}$ as a function of the wall-normal distance is shown in figure 10(*a*) for the different values of Ri_τ. We observe that $\mathcal{N}$ is large at the centre of the channel – and peaks at the centreline – due to the sharpening of the mean temperature profile

therein (figure 5), while it is rather small in the remaining part of the channel. Note that the behaviour of $\mathcal{N}$ in the proximity of the wall – shaded area in figure 10(*b*) – is not particularly important for the present discussion, since the temperature gradient in that region is mostly influenced by the presence of the boundary rather than by buoyancy. In the framework of the present discussion, it is interesting to look at the time-averaged premultiplied streamwise energy spectra of wall-normal velocity fluctuations, $k_x E_{u_z'^2}(k_x)$, at the channel centreline (Iida *et al.* 2002; Yeo *et al.* 2009; Zonta *et al.* 2012*b*). Results are presented in figure 10(*b*) for the different values of Ri_τ. We consider in particular the case $Ri_\tau = 300$, for which stratification is more important. We note that $k_x E_{u_z'^2}(k_x)$ develops a peak – which is not observed for $Ri_\tau = 0$ – at the dimensionless wavenumber $\hat{k}_x = k_x h \approx 5$ (where k_x is the wavenumber in dimensional form). We can hypothesize that this peak is due to the presence of IGWs, which induce vertical velocity fluctuations at the frequency $\mathcal{N}$ (Zonta *et al.* 2012*b*). To demonstrate this relationship, we assume that IGWs move in the streamwise direction with the mean centreline velocity, u_{IGW}. For $Ri_\tau = 300$, $u_{IGW}^+ \simeq 47$ (or, in dimensional form, $u_{IGW} = u_\tau u_{IGW}^+ \simeq 1$ m s^{-1}). The corresponding frequency of such waves is $\omega_{IGW} = u_{IGW} \times k_x/2\pi \simeq 1$ s^{-1}. Considering now the value of the buoyancy frequency at the channel centreline, we get $\mathcal{N} \simeq 38$ or, in dimensional form, $N = \mathcal{N} u_\tau/h \simeq 1$ s^{-1}, in close agreement with the previous estimate. Also shown in figure 10(*a*) is the range of frequency peaks, which correlates well with the range of wavenumber peaks shown in figure 10(*b*). The previous estimate is based on an oversimplified scenario, in which IGWs are monochromatic waves that travel at the advection velocity and are characterized by the frequency N. However, it is known (Staquet & Sommeria 2002) that the frequency of IGWs obeys the dispersion relation

$$\omega = \pm N \cos\phi = \pm N \frac{\sqrt{k_x^2 + k_y^2}}{\sqrt{k_x^2 + k_y^2 + k_z^2}}, \tag{3.7}$$

in which the wave vector $\boldsymbol{k} = (k_x, k_y, k_z)$ is not necessarily directed along x, and can have an angle ϕ to the horizontal plane. From (3.7), it clearly emerges that IGWs are characterized by frequencies in the range $0 < \omega \leqslant N$. In addition, due to the advection velocity u_{IGW} at the channel centre, the observed wave frequency is modified by the Doppler shift, which takes the form $\omega_{DS} = u_{IGW}\hat{k}_x$. Therefore, the frequency of IGWs can be expressed by the relation

$$\omega = \omega_{DS} \pm N \cos\phi = u_{IGW}\hat{k}_x \pm N \cos\phi. \tag{3.8}$$

From (3.8), and under the assumption of $\cos\phi = 1$, it emerges that the observed peak wavenumber $\hat{k}_x$ in figure 10(*b*) corresponds to the Doppler shift $u_{IGW}\hat{k}_x = N$. This result seems consistent with the recent analysis of Maffioli, Delache & Godeferd (2020), in which – employing spatio-temporal analysis of an unbounded stratified flow – it was shown that the dominant contributions to the wave energy in stratified turbulence come from frequencies close to N.

Using the buoyancy frequency N, we can calculate the gradient Richardson number as

$$Ri_g = \frac{N^2}{S^2} = \frac{-g\beta \dfrac{\partial\langle\theta\rangle}{\partial z}}{\left(\dfrac{\partial\langle u_x\rangle}{\partial z}\right)^2}, \tag{3.9}$$
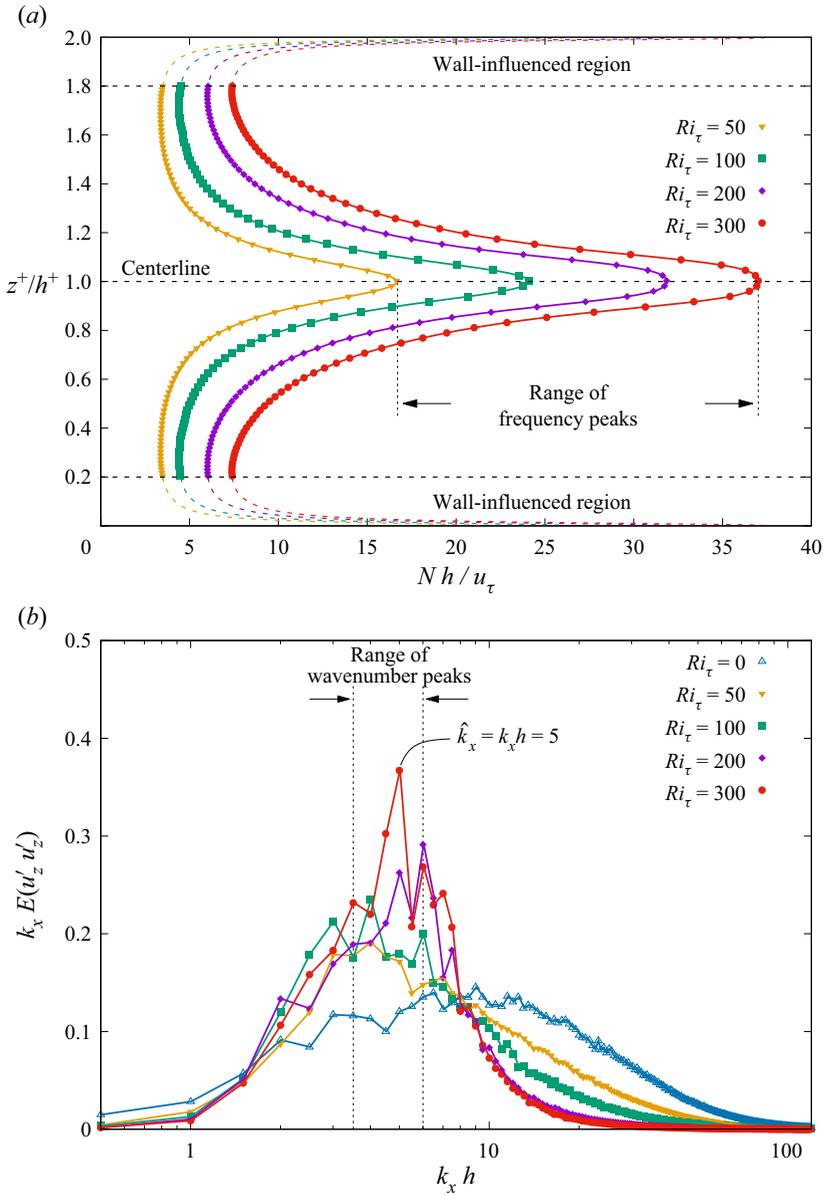
(*a*)

(*b*)

Figure 10. (*a*) Wall-normal behaviour of the mean Brunt–Väisälä frequency N for the different cases of stratified turbulence ($Ri_\tau = 50$, $Ri_\tau = 100$, $Ri_\tau = 200$ and $Ri_\tau = 300$). (*b*) Time-averaged premultiplied streamwise energy spectra of wall-normal velocity fluctuations $k_x E(u'_z u'_z)$ evaluated on a wall-parallel (x–y) plane located at the channel centre.

where S is the mean shear rate. The gradient Richardson number is a measure of the relative importance of the buoyant consumption of turbulence, N^2, compared with the shear production of turbulence, S^2. In the literature (Miles 1961; Rohr *et al.* 1988; Holt, Koseff & Ferziger 1992; Piccirillo & Van Atta 1997), $Ri_g \simeq 0.25$ has been identified as a critical threshold to evaluate the flow structure in unbounded stratified flows, where Ri_g is uniform in space. For $Ri_g \simeq 0.25$, turbulence does not grow or decay. At larger
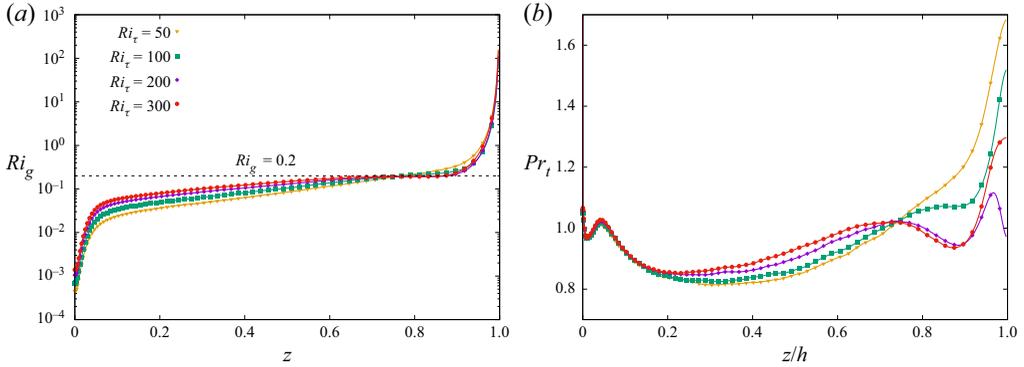
Figure 11. Wall-normal behaviour of the gradient Richardson number Ri_g (*a*) and of the turbulent Prandtl number Pr_t (*b*) for the different values of Ri_τ. The threshold value $Ri_g = 0.2$ is also explicitly shown in panel (*a*) (dashed line).

Ri_g, turbulence decays, while at smaller Ri_g turbulence grows. Naturally, in wall-bounded flows, Ri_g varies in the wall-normal direction from small values close to the wall, to large values close to the centre of the channel. This is represented in figure 11, where we plot Ri_g in logarithmic scale as a function of the dimensionless wall-normal distance, for different Ri_τ. Current results are in good agreement with previous observations (Armenio & Sarkar 2002; Taylor, Sarkar & Armenio 2005; García-Villalba & del Álamo 2011; Zonta *et al.* 2012*b*), showing in particular the sharp increase of Ri_g around $Ri_g \simeq 0.2$. This sharp increase, which occurs at the channel centre (where $\partial \langle \theta \rangle / \partial z$ is large while $\partial \langle u_x \rangle / \partial z \to 0$) identifies the region of the channel in which buoyant consumption of turbulence dominates over shear production of turbulence, and sets the boundaries where IGWs are observed ($z^+/h^+ > 0.8$). Based on the previous observations, it seems reasonable to set the value $Ri_g = 0.2$ as the critical threshold above which turbulence is significantly damped by buoyancy in wall-bounded stratified turbulence.

A further crucial aspect of stratified turbulence is the evaluation of irreversible mixing of momentum and energy (Fernando 1991; Ivey, Winters & Koseff 2008). A common approach to evaluating mixing in stratified turbulence is to rely on the concept of turbulent eddy viscosity, $\mathcal{K}_m$, and diffusivity, $\mathcal{K}_\theta$, which are defined as (Pope 2000)

$$\mathcal{K}_m = \frac{\langle u'w' \rangle}{\dfrac{\partial \langle u \rangle}{\partial z}}, \quad \mathcal{K}_\theta = \frac{\langle \theta'w' \rangle}{\dfrac{\partial \langle \theta \rangle}{\partial z}}. \tag{3.10a,b}$$

The ratio between $\mathcal{K}_m$ and $\mathcal{K}_\theta$ is usually referred to as turbulent Prandtl number (Launder & Spalding 1972), and can be written in dimensionless form as

$$Pr_T = \frac{\langle u'w' \rangle \dfrac{\partial \langle \theta \rangle}{\partial z}}{\langle w'\theta' \rangle \dfrac{\partial \langle u \rangle}{\partial z}}. \tag{3.11}$$

The evaluation of Pr_T as a function of the distance from the wall and for different stratification levels (i.e. different Ri_τ), is a major aspect in the field of turbulence modelling (Grachev *et al.* 2007; Venayagamoorthy & Stretch 2010). In figure 11(*b*) we plot Pr_T as a function of z^+/h^+. Near the boundary, and regardless of Ri_τ, we observe that $Pr_T \simeq 1$. Above $z^+/h^+ \simeq 0.2$, there is slight dependence of Pr_T on Ri_τ, but Pr_T remains bounded in
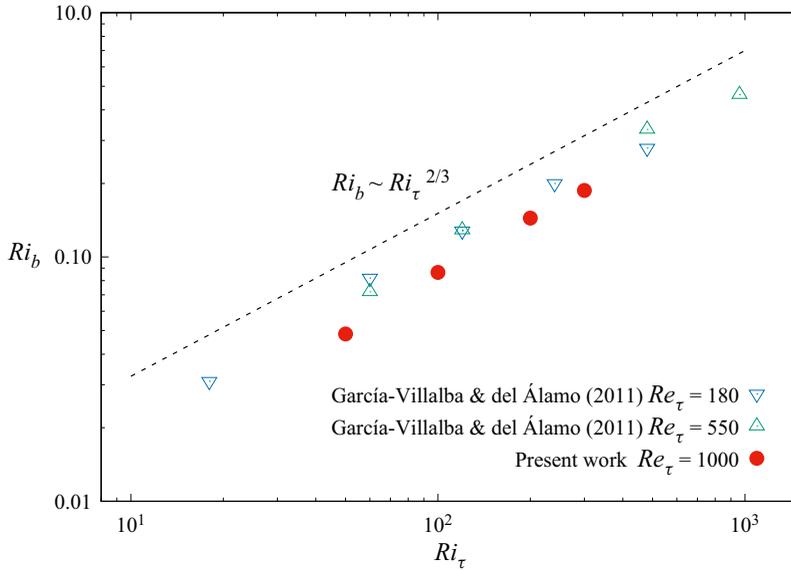
945 A3-20

Figure 12. Bulk Richardson number, Ri_b, as a function of the shear Richardson number, Ri_τ, for the present simulations at $Re_\tau = 1000$, and for previous simulations at $Re_\tau = 180$ and $Re_\tau = 550$ (García-Villalba & del Álamo 2011). The proposed scaling $Re_b \sim Ri_\tau^{2/3}$ is also explicitly indicated.

the range $0.8 < Pr_T < 1.2$. At the channel centre, where stratification effects are stronger, the behaviour of Pr_T does not have a clear trend for increasing Ri_τ, although Pr_T does not depart much from unity. We therefore conclude that the assumption $Pr_T \approx 1$, customarily taken in turbulence modelling (Laskowski *et al.* 2007; Zonta 2013), seems a reasonable choice for mild to moderate stratification levels.

3.5. *Macroscopic characterization of the flow: Ri_b, C_f, Nu*

Although the shear Richardson number Ri_τ is customarily used to characterize the flow in numerical simulations of wall-bounded stratified turbulence (Zonta & Soldati 2018), its use in experiments/field measurements is much more limited. The reason is the difficult experimental evaluation of the shear velocity, which in turn requires the measurement of the shear stress at the wall. As a consequence, in many experiments the bulk Richardson number $Ri_b = \beta(\Delta T/2)gh/(2u_b^2)$ is usually preferred, since the bulk velocity u_b is an easily accessible quantity. To draw a link between simulations and experiments/field measurements, it is interesting to evaluate the behaviour of the bulk Richardson number Ri_b, as a function of the shear Richardson number Ri_τ. This behaviour is shown in figure 12. Present results (filled symbols, •, red), which are plotted together with literature results obtained at lower Re_τ (open symbols), confirm previous indications that $Ri_b \propto Ri_\tau^{2/3}$. In view of its independence on Re_τ – at least over approximately one decade, from $Re_\tau = 180$ up to $Re_\tau = 1000$ – the proposed Ri_b scaling seems a general property of the flow that can be used as a robust parametrization tool, as will be shown below.

Perhaps the most important quantities to be monitored in wall-bounded stratified turbulence are the overall momentum and heat transfer rates, which are commonly quantified in terms of the friction factor C_f – shear stress to kinetic energy ratio – and
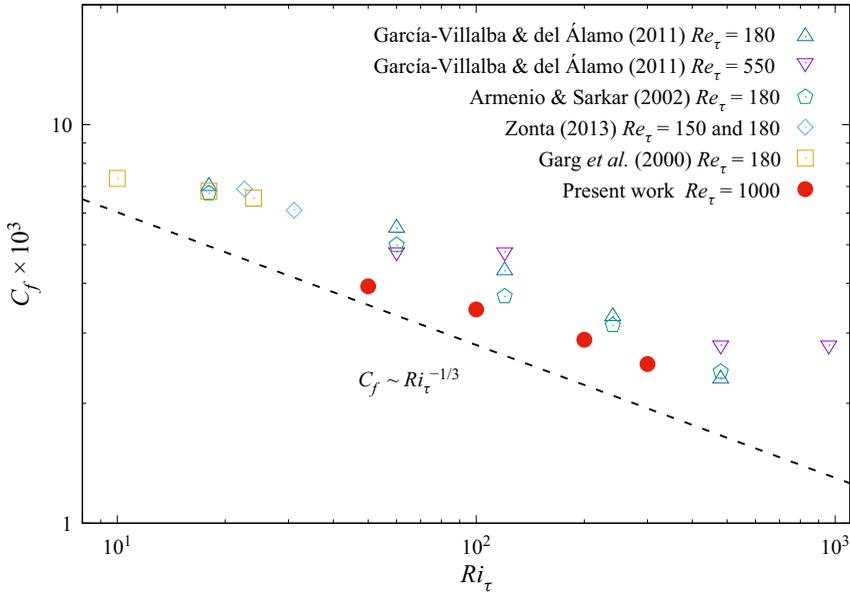
Figure 13. Friction factor C_f as a function of the shear Richardson number Ri_τ. Results of present study (filled symbols) are shown together with results obtained in previous studies (Garg *et al.* 2000; Armenio & Sarkar 2002; García-Villalba & del Álamo 2011; Zonta *et al.* 2012*b*; Zonta 2013). The proposed scaling $C_f \sim Ri_\tau^{-1/3}$ is also explicitly indicated.

by the Nusselt number Nu – convective to conductive heat transfer ratio – as

$$\left.\begin{aligned} C_f &= \frac{2\tau_w}{\rho u_b^2}, \\ Nu &= \frac{2q_w h}{\lambda \Delta T}. \end{aligned}\right\} \tag{3.12}$$

Results obtained from the present simulations are shown by filled symbols (●, red) in figures 13–14, together with the results obtained in previous studies (Garg *et al.* 2000; Armenio & Sarkar 2002; García-Villalba & del Álamo 2011; Zonta *et al.* 2012*b*; Zonta 2013). Focusing on C_f (figure 13), it is clear that an increase of stratification (increase of Ri_τ) reduces the wall-normal momentum transfer, via the reduction of wall-normal turbulent transport and via the corresponding increase of the volume flowrate (keeping the imposed pressure gradient constant). Interestingly, recalling that $Ri_b \propto Ri_\tau^2/3$ (see figure 12), and considering that $C_f/4 = Ri_b/Ri_\tau$, we obtain $C_f \sim Ri_\tau^{-1/3}$ (García-Villalba & del Álamo 2011). This scaling law, which is shown in figure 13 together with the reported numerical results, predicts fairly well the behaviour of C_f for a broad range of Ri_τ, with some departure observed only at very large stratification levels (when local flow laminarization is likely to appear).

The fair collapse observed for C_f is not recovered for the Nusselt Number Nu (not shown in figure 14). Interestingly, when rescaled by $Re_\tau^{-2/3}$, the collected results collapse nicely (figure 14) and scale as $Nu \times Re_\tau^{-2/3} \sim Ri_\tau^{-1/3}$ (therefore giving $Nu \times Re_\tau^{-2/3} \sim C_f$). The proposed scaling differs from classical analogies widely used in the literature – such as the Chilton and Colburn one $C_f/2 = Nu \times Re^{-1} \times Pr^{-1/3}$ (Bird, Stewart & Lightfoot 2007) – to relate heat, mass and momentum transfer coefficients in forced convection phenomena.
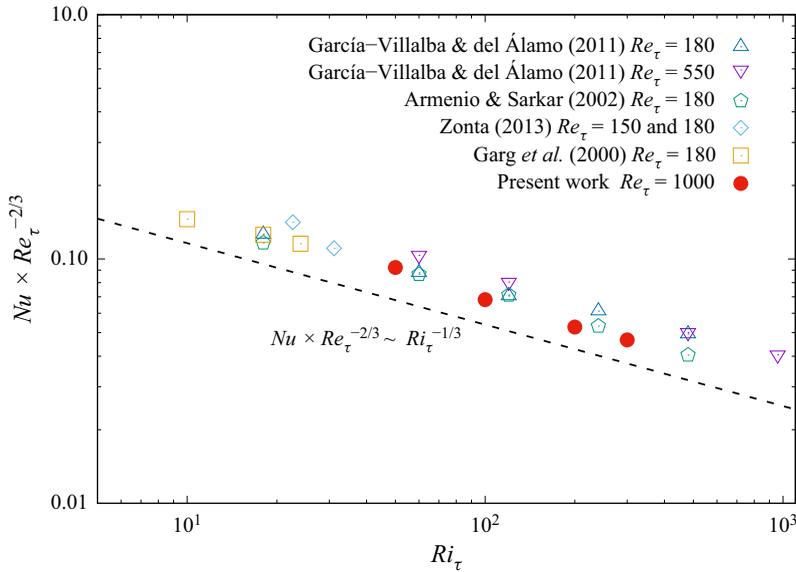
945 A3-22

Figure 14. Rescaled Nusselt number $Nu \times Re_\tau^{-2/3}$ as a function of the shear Richardson number Ri_τ. Results of present study (filled symbols) are shown together with results obtained in previous studies (Garg *et al.* 2000; Armenio & Sarkar 2002; García-Villalba & del Álamo 2011; Zonta *et al.* 2012*b*; Zonta 2013). Note that the values of Nu in Zonta *et al.* (2012*b*) and Zonta (2013), obtained at $Pr = 3$, have been rescaled by $Pr^{1/3}$. The proposed scaling $Nu \times Re_\tau^{-2/3} \sim Ri_\tau^{-1/3}$ is also explicitly indicated.

It is reasonable to expect that the interaction between buoyancy and momentum modifies the main transport processes in a non-trivial way that is hard to predict by simplified assumptions. An in-depth analysis and a corresponding accurate parametrization of the actual flow field are therefore required to shed some light on the proposed scaling, which, however, appears rather robust.

4. Conclusions

We analysed the flow physics of stratified wall-bounded turbulence at high Reynolds number by running a series of DNS of stably stratified channel flow at fixed Reynolds and Prandtl number ($Re_\tau = 1000$ and $Pr = 0.71$, respectively) and at different values of the shear Richardson number, up to $Ri_\tau = 300$. From a physical viewpoint, the simulation set-up can be assimilated to the flow of air inside a channel of height $2h \sim 1.5$ m at a reference bulk Reynolds number (based on h) $Re_b = 2 \times 10^4$ and subject to a wall-to-wall temperature difference up to ≈ 10 K.

For the considered range of Ri_τ, active turbulence is sustained close to the walls, where the strong mean shear generates small-scale vorticity that is not affected by the imposed stratification. Farther from the wall, where vortices and flow structures are larger, stratification has an important influence. Even for low-to-moderate levels of stratification, buoyancy effects dominate in this region, as the mean shear is small (the channel centre is a symmetry plane). Interestingly, although temperature and wall-normal velocity fluctuations are very large at the channel centre, their correlation – which represents the buoyancy flux – decreases so much that, for $Ri_\tau \geqslant 200$, it becomes nearly zero. We show that this behaviour is due to the presence of a $\approx \pi/2$ phase shift between the temperature fluctuations and the wall-normal velocity fluctuations that causes no

correlation between the two signals. These findings are consistent with the presence of IGWs at the channel centre. It is worth observing that, although hypothesized in previous works (Komori *et al.* 1983; Armenio & Sarkar 2002), we did not find evidence of any mean counter-gradient heat flux, even at the largest stratification considered here. These results, however, can supply further motivation to examine this flow at even higher stratification levels. Finally, we focused on the behaviour of the overall momentum and heat transfer rates, represented by the friction factor, C_f, and the Nusselt number, Nu, respectively. We showed that the friction factor scales as $C_f \sim Ri_\tau^{-1/3}$, while the Nusselt number scales as $Nu \times Re_\tau^{-2/3} \sim Ri_\tau^{-1/3}$. We remark here that the current large-scale dataset of stably stratified channel turbulence at $Re_\tau = 1000$ are expected to help LES and Reynolds-averaged Navier–Stokes similations to build efficient and reliable subgrid-scale and closure models for wall-bounded buoyancy-influenced turbulence (Lazeroms *et al.* 2013).

Declaration of interests. The authors report no conflict of interest.

Author ORCIDs.

- Francesco Zonta https://orcid.org/0000-0002-3849-315X;
- Pejman Hadi Sichani https://orcid.org/0000-0003-1440-3479;
- Alfredo Soldati https://orcid.org/0000-0002-7515-7147.

REFERENCES

ALCÁNTARA-ÁVILA, F., HOYAS, S. & JEZABEL PÉREZ-QUILES, M. 2021 Direct numerical simulation of thermal channel flow for $Re_\tau = 5000$ and $Pr = 0.71$. *J. Fluid Mech.* **916**, A29.

ARMENIO, V. & SARKAR, S. 2002 An investigation of stably stratified turbulent channel flow using large-eddy simulation. *J. Fluid Mech.* **459**, 1–42.

ARYA, S.P.S. 1975 Buoyancy effects in an horizontal flat-plane boundary layer. *J. Fluid Mech.* **68**, 321–343.

BIRD, R.B., STEWART, W.E. & LIGHTFOOT, E.N. 2007 *Transport Phenomena*. John Wiley and Sons.

BOLGIANO, R. 1959 Turbulent spectra in a stable stratified atmosphere. *J. Geophys. Res.* **64**, 2226–2229.

BRETHOUWER, G., DUGUET, Y. & SCHLATTER, P. 2012 Turbulent-laminar coexistence in wall flows with coriolis, buoyancy or lorentz forces. *J. Fluid Mech.* **704**, 137–172.

CAULFIELD, C.P. 2021 Layering, instabilities, and mixing in turbulent stratified flows. *Annu. Rev. Fluid Mech.* **53**, 113–145.

DEUSEBIO, E., CAULFIELD, C.P. & TAYLOR, J.R. 2015 The intermittency boundary in stratified plane Couette flow. *J. Fluid Mech.* **781**, 298–329.

DOSTAL, V., HEJZLAR, P. & DRISCOLL, M.J. 2006 The supercritical carbon dioxide power cycle: comparison to other advanced power cycles. *Nucl. Technol.* **154**, 283–301.

FERNANDO, H.J.S. 1991 Turbulent mixing in stratified fluids. *Annu. Rev. Fluid Mech.* **23**, 455–493.

FERZIGER, J.H., KOSEFF, J.R. & MONISMITH, S.G. 2002 Numerical simulation of geophysical turbulence. *Comput. Fluids* **31**, 557–568.

GAGE, K.S. & REID, W.H. 1968 The stability of thermally stratified plane Poiseuille flow. *J. Fluid Mech.* **33**, 21–32.

GARCÍA-VILLALBA, M. & DEL ÁLAMO, J.C. 2011 Turbulence modification by stable stratification in channel flow. *Phys. Fluids* **23**, 045104.

GARG, R.P., FERZIGER, J.H., MONISMITH, S.G. & KOSEFF, J.R. 2000 Stably stratified turbulent channel flows. I. Stratification regimes and turbulence suppression mechanism. *Phys. Fluids* **12**, 2569–2594.

GRACHEV, A.A., ANDREAS, E.L., FAIRALL, C.W., GUEST, P.S. & PERSSON, P.O.G. 2007 On the turbulent Prandtl number in the stable atmospheric boundary layer. *Boundary-Layer Meteorol.* **125** (2), 329–341.

HADI SICHANI, P., MARCHIOLI, C., ZONTA, F. & SOLDATI, A. 2020 Shear effects on scalar transport in double diffusive convection. *Trans. ASME J. Fluids Engng* **142**, 121105.

HE, P. 2016 A high order finite difference solver for massively parallel simulations of stably stratified turbulent channel flows. *Comput. Fluids* **127**, 161–173.

HOLT, S.E., KOSEFF, J.R. & FERZIGER, J.H. 1992 A numerical study of the evolution and structure of homogeneous stably stratified sheared turbulence. *J. Fluid Mech.* **237**, 499–539.

HUISMAN, S.G., VAN GILS, D.P.M., GROSSMANN, S., SUN, C. & LOHSE, D. 2012 Ultimate turbulent Taylor–Couette flow. *Phys. Rev. Lett.* **108**, 024501.

IIDA, O., KASAGI, N. & NAGANO, Y. 2002 Direct numerical simulation of turbulent channel flow under stable density stratification. *Intl J. Heat Mass Transfer* **45**, 1693–1703.

IVEY, G.N., WINTERS, K.B. & KOSEFF, J.R. 2008 Density stratification, turbulence, but how much mixing? *Annu. Rev. Fluid Mech.* **40**, 169–184.

KOMORI, S., UEDA, H., OGINO, F. & MIZUSHINA, T. 1983 Turbulence structure in stably stratified open-channel flow. *J. Fluid Mech.* **130**, 13–26.

LACASCE, J.H. & BOWER, A. 2000 Relative dispersion in the subsurface North Atlantic. *J. Mar. Res.* **58**, 863–894.

LASKOWSKI, G.M., KEARNEY, S.P., EVANS, G. & GREIF, R. 2007 Mixed convection heat transfer to and from a horizontal cylinder in cross–flow with heating from below. *Intl J. Heat Fluid Flow* **28**, 454–468.

LAUNDER, B.E. & SPALDING, D.B. 1972 *Mathematical Models of Turbulence*. Academic Press.

LAZEROMS, W.M.J., BRETHOUWER, G., WALLIN, S. & JOHANSSON, A.V. 2013 An explicit algebraic Reynolds-stress and scalar-flux model for stably stratified flows. *J. Fluid Mech.* **723**, 91–125.

LOVECCHIO, S., ZONTA, F. & SOLDATI, A. 2014 Influence of thermal stratification on the surfacing and clustering of floaters in free surface turbulence. *Adv. Water Resour.* **72**, 22–31.

MAFFIOLI, A., DELACHE, A. & GODEFERD, F.S. 2020 Signature and energetics of internal gravity waves in stratified turbulence. *Phys. Rev. Fluids* **5**, 114802.

MAHRT, L. 2014 Stably stratified atmospheric boundary layers. *Annu. Rev. Fluid Mech.* **46**, 23–45.

MILES, J.W. 1961 On the stability of heterogeneous shear flows. *J. Fluid Mech.* **10**, 496–508.

MOESTAM, R. & DAVIDSON, L. 2005 Numerical simulations of thermocline in a pressure-driven flow between two infinite horizontal plates. *Phys. Fluids* **17**, 075109.

MONIN, A.S. & OBUKHOV, A.M. 1954 Basic laws of turbulent mixing in the surface layer of the atmosphere. *Contrib. Geophys. Inst. Acad. Sci. USSR* **151**, 163–187.

OHYA, Y., NEFF, D. & MERONEY, R. 1997 Turbulence structure in a stratified boundary layer under stable conditions. *Boundary-Layer Meteorol.* **83**, 139–161.

ORTIZ-SUSLOW, D.G., KALOGIROS, J., YAMAGUCHI, R. & WANG, Q. 2021 An evaluation of the constant flux layer in the atmospheric flow above the wavy air-sea interface. *J. Geophys. Res.: Atmos.* **126**, e2020JD032834.

PICCIRILLO, P. & VAN ATTA, C.W. 1997 The evolution of a uniformly sheared thermally stratified turbulent flow. *J. Fluid Mech.* **334**, 61–86.

PITLA, S.S., ROBINSON, D.M., GROLL, E.A. & RAMADHYANI, S. 2006 Heat transfer from supercritical carbon dioxide in tube flow: a critical review. *HVAC&R Res.* **4**, 281–301.

POPE, S.B. 2000 *Mathematical Models of Turbulence*. Cambridge University Press.

ROHR, J.J., ITSWEIRE, E.C., HELLAND, K.N. & VAN ATTA, C.W. 1988 Growth and decay of turbulence in a stably stratified shear flow. *J. Fluid Mech.* **195**, 77–111.

SHANG, X.-D., TONG, P. & XIA, K.-Q. 2005 Test of steady-state fluctuation theorem in turbulent Rayleigh–Bénard convection. *Phys. Rev.* E **72** (1), 015301.

STAQUET, C. & SOMMERIA, J. 2002 Internal gravity waves: from instabilities to turbulence. *Annu. Rev. Fluid Mech.* **34**, 559–593.

TAYLOR, J.R., SARKAR, S. & ARMENIO, V. 2005 Large eddy simulation of stably stratified open channel flow. *Phys. Fluids* **17**, 116602.

TENNEKES, H. & LUMLEY, J. 1972 *A First Course in Turbulence*. MIT.

VENAYAGAMOORTHY, S.K. & STRETCH, D.D. 2010 On the turbulent Prandtl number in homogeneous stably stratified turbulence. *J. Fluid Mech.* **644**, 359–369.

WILLIAMS, O., HOHMAN, T., VAN BUREN, T., BOU-ZEID, E. & SMITS, A.J. 2017 The effect of stable thermal stratification on turbulent boundary layer statistics. *J. Fluid Mech.* **812**, 1039–1075.

WILLIAMSON, N., ARMFIELD, S.W., KIRKPATRICK, M.P. & NORRIS, S.E. 2015 Transition to stably stratified states in open channel flow with radiative surface heating. *J. Fluid Mech.* **766**, 528–555.

YEO, K., KIM, B.G. & LEE, C. 2009 Eulerian and lagrangian statistics in stably stratified turbulent channel flows. *J. Turbul.* **10**, 1–26.

ZONTA, F. 2013 Nusselt number and friction factor in thermally stratified turbulent channel flow under non-Oberbeck–Boussinesq conditions. *Intl J. Heat Fluid Flow* **44**, 489–494.

ZONTA, F. & CHIBBARO, S. 2016 Entropy production and fluctuation relation in turbulent thermal convection. *Europhys. Lett.* **114**, 50011.

ZONTA, F., MARCHIOLI, C. & SOLDATI, A. 2012*a* Modulation of turbulence in forced convection by temperature-dependent viscosity. *J. Fluid Mech.* **697**, 150–174.

ZONTA, F., ONORATO, M. & SOLDATI, A. 2012*b* Turbulence and internal waves in stably-stratified channel flow with temperature-dependent fluid properties. *J. Fluid Mech.* **697**, 175–203.

ZONTA, F. & SOLDATI, A. 2014 Effect of temperature dependent fluid properties on heat transfer in turbulent mixed convection. *Trans. ASME J. Heat Transfer* **136** (2), 022501.

ZONTA, F. & SOLDATI, A. 2018 Stably stratified wall-bounded turbulence. *Appl. Mech. Rev.* **70**, 040801.